Journal of Statistical Physics, Vol. 88, Nos. 3/4, 1997

Lattice Boltzmann Model for the Incompressible Navier–Stokes Equation

Xiaoyi He[1,2] **and Li-Shi Luo**[1,3]

Received September 28, 1995; final February 21, 1997

In this paper a lattice Boltzmann (LB) model to simulate incompressible flow is developed. The main idea is to explicitly eliminate the terms of $o(M^2)$, where M is the Mach number, due to the density fluctuation in the existing LB models. In the proposed incompressible LB model, the pressure p instead of the mass density ρ is the independent dynamic variable. The incompressible Navier–Stokes equations are derived from the incompressible LB model via Chapman–Enskog procedure. Numerical results of simulations of the plane Poiseuille flow driven either by pressure gradient or a fixed velocity profile at entrance as well as of the 2D Womersley flow are presented. The numerical results are found to be in excellent agreement with theory.

KEY WORDS: Lattice Boltzmann method; incompressible Navier–Stokes equation; Poiseuille flow; Womersley flow.

1. INTRODUCTION

In the last decade or so, the lattice Boltzmann (LB) method has emerged as a new and effective numerical technique of computational fluid dynamics (CFD).[1-5] Modeling of the incompressible Navier–Stokes equation is among many of its wide applications. Indeed, the lattice Boltzmann equation (LBE) was first proposed to simulate the incompressible Navier–Stokes equations.[1] The incompressible Navier–Stokes equations can

[1] Complex Systems Group (T-13), MS-B213, Theoretical (T) Division, Los Alamos National Laboratory, Los Alamos, New Mexico 87545.

[2] Center for Nonlinear Studies (CNLS), MS-B258, Los Alamos National Laboratory, Los Alamos, New Mexico 87545.

[3] ICASE, MS 403, NASA Langley Research Center, 6 North Dryden St., Bldg. 1298, Hampton, Virginia 23681-0001; e-mail: luo@icase.edu.

0022-4715/97/0800-0927$12.50/0

be derived from the lattice Boltzmann equation through the Chapman–Enskog procedure if the density fluctuation is *assumed* to be negligible. Unfortunately, this is not always the case in numerical simulations by using LBE method. The compressible effect in the existing LBE models may produce some serious errors in numerical simulations. There have been efforts to reduce or to eliminate the compressible effect in the LBE method.[6–8] However, the results are not entirely satisfactory mainly for the reason that the existing models for incompressible flow are only valid for steady flows in theory. Therefore, it is still necessary to improve the LBE method for simulations of the incompressible Navier–Stokes equations in general, especially for unsteady flows.

Ideally, the incompressibility can be achieved only when the mass density becomes a constant. However, it is practically impossible to maintain a constant density in lattice Boltzmann models. Theoretically the lattice Boltzmann equation always simulates the compressible Navier–Stokes equation instead of the incompressible one, because the spatial density variation is not zero in LBE simulations. In order to correctly simulate the incompressible Navier–Stokes equation in practice, one must ensure that the Mach number, M, and the density variation, $\delta\rho$, are of the order $O(\varepsilon)$ and $O(\varepsilon^2)$, respectively, where ε is the Knudsen number.[9] However, in numerical simulations such as flow through porous media, a pressure gradient is applied to drive the system, and the pressure gradient is established by maintaining a density gradient in the system. Moreover, this is the only way to implement the boundary condition of a pressure gradient in the system by using the method of the LBE or the lattice gas automata (LGA), because of the simple ideal gas equation of state of the system, and because pressure is not an independent dynamical variable in the LBE or LGA methods. Under this circumstance, the assumption of constant density is no longer valid and the magnitude of the density variation may be rather significant. This would inevitably bring in an error in the LBE simulations of the incompressible Navier–Stokes equations.

Historically, in the context of the lattice gas automata (LGA)[6] the incompressibility is achieved by rewriting the Navier–Stokes equation in terms of the momentum density $\boldsymbol{j} \equiv \rho \boldsymbol{u}$ rather than the velocity $\boldsymbol{u}$. The same idea has been applied to LBE models for Burgers' equation[7] and the Navier–Stokes equation.[8] Although this approach seems to provide some good numerical results for steady flows, its validity for unsteady flow is unknown.

It is well known that the lattice Boltzmann method is only applicable to the low Mach number hydrodynamics, because a small velocity expansion is (*implicitly*) used in derivation of the Navier–Stokes equation from the lattice Boltzmann equation. It should be noted that the small Mach

number limit is equivalent to the incompressible limit. Thus, it should be possible to develop a lattice Boltzmann model to simulate the incompressible Navier–Stokes equation properly. In this paper, a lattice Boltzmann model for the incompressible Navier–Stokes equation is developed. The basic idea is to explicitly eliminate the compressible effect by neglecting the terms of higher order Mach number, specifically, the terms of order $o(M^2)$. This paper is organized as follows. Section II proposes an incompressible lattice Boltzmann model and derives the incompressible Navier–Stokes equation from the model. The validity of the proposed model is also briefly discussed. Section III provides numerical results of simulations of the plane Poiseuille flow and the 2-D Womersley flow using the incompressible Boltzmann model. The Poiseuille flow is a steady flow, whereas the Womersley flow is a unsteady one. Section IV discusses the results and concludes this paper.

II. THEORY

In the following analysis, the derivation of the incompressible Navier–Stokes equation is presented via an example of the 9-bit lattice BGK model in two-dimensional space. It should be pointed out that the approach is applicable to other lattice Boltzmann models in either two- or three-dimensional space in general.

The 9-bit lattice BGK model evolves on the two-dimensional square lattice space with the following 9 discrete velocities:

$$\boldsymbol{e}_\alpha = \begin{cases} (0, 0) & \alpha = 0 \\ (\cos[(\alpha-1)\,\pi/2, \sin[(\alpha-1)\,\pi/2])\,c & \alpha = 1, 2, 3, 4 \\ (\cos[(\alpha-5)\,\pi/2+\pi/4], \sin[(\alpha-5)\,\pi/2+\pi/4])\,\sqrt{2}\,c & \alpha = 5, 6, 7, 8 \end{cases} \tag{1}$$

where $c = \delta_x/\delta_t$, and δ_x and δ_t are the lattice constant and the time step size, respectively. Figure 1 show the velocities of the 9-bit model. The evolution equation of the system is

$$f_\alpha(\boldsymbol{x} + \boldsymbol{e}_\alpha \delta_t, t + \delta_t) - f_\alpha(\boldsymbol{x}, t) = -\frac{1}{\tau}[f_\alpha(\boldsymbol{x}, t) - f_\alpha^{(\mathrm{eq})}(\boldsymbol{x}, t)] \tag{2}$$

where τ is the dimensionless collision relaxation time, and the equilibrium distribution function, $f_\alpha^{(\mathrm{eq})}$, is given by:

$$f_\alpha^{(\mathrm{eq})} = w_\alpha \rho \left[1 + 3\frac{(\boldsymbol{e}_\alpha \cdot \boldsymbol{u})}{c^2} + \frac{9}{2}\frac{(\boldsymbol{e}_\alpha \cdot \boldsymbol{u})^2}{c^4} - \frac{3}{2}\frac{\boldsymbol{u}^2}{c^2} \right] \tag{3}$$

with the weight coefficient

$$w_\alpha = \begin{cases} \frac{4}{9} & \alpha = 0 \\ \frac{1}{9} & \alpha = 1, 2, 3, 4 \\ \frac{1}{36} & \alpha = 5, 6, 7, 8 \end{cases}$$

It is noted that, in the above equilibrium distribution function,

$$\frac{|\boldsymbol{u}|}{c} \approx M$$

It is well understood that in an incompressible fluid the density is (approximantly) a constant, say ρ_0, and the density fluctuation, $\delta\rho$, should be of the order $O(M^2)$ in the limit of $M \to 0$.[9] If we explicitly substitute $\rho = \rho_0 + \delta\rho$ into the equilibrium distribution function, $f_\alpha^{(\mathrm{eq})}$, and neglect the terms proportional to $\delta\rho(\boldsymbol{u}/c)$, and $\delta\rho(\boldsymbol{u}/c)^2$, which are of the order $O(M^3)$ or higher, then the equilibrium density distribution function becomes

$$f_\alpha^{(\mathrm{eq})}(\boldsymbol{x}, t) = w_\alpha \left\{ \rho + \rho_0 \left[3\frac{(\boldsymbol{e}_\alpha \cdot \boldsymbol{u})}{c^2} + \frac{9}{2}\frac{(\boldsymbol{e}_\alpha \cdot \boldsymbol{u})^2}{c^4} - \frac{3}{2}\frac{\boldsymbol{u}^2}{c^2} \right] \right\} \tag{4}$$

The above distribution function is the equilibrium distribution function of the incompressible lattice Boltzmann model. Clearly, the remaining terms in the above equation are of the order $O(M^2)$ or lower order. It should be stressed that the approximation made here is fully consistent with the second order small velocity expansion (or low Mach number expansion up to the second order) in the Chapman–Enskog analysis of LBE models.

Since it is a common practice to use the pressure, p, as an independent variable in the incompressible Navier–Stokes equation, we introduce a local pressure distribution function

$$p_\alpha \equiv c_s^2 f_\alpha$$

where c_s is the sound speed, and $c_s = c/\sqrt{3}$ for the 9-bit model. Accordingly, the evolution equation of the LBE system, Eq. (2), becomes

$$p_\alpha(\boldsymbol{x} + \boldsymbol{e}_\alpha \delta_t, t + \delta_t) - p_\alpha(\boldsymbol{x}, t) = -\frac{1}{\tau}[p_\alpha(\boldsymbol{x}, t) - p_\alpha^{(\mathrm{eq})}(\boldsymbol{x}, t)] \tag{5}$$

where

$$p_\alpha^{(\mathrm{eq})} \equiv c_s^2 f_\alpha^{(\mathrm{eq})} = w_\alpha \left\{ p + p_0 \left[3\frac{(\boldsymbol{e}_\alpha \cdot \boldsymbol{u})}{c^2} + \frac{9}{2}\frac{(\boldsymbol{e}_\alpha \cdot \boldsymbol{u})^2}{c^4} - \frac{3}{2}\frac{\boldsymbol{u}^2}{c^2} \right] \right\} \tag{6}$$

$p = c_s^2 \rho$, and $p_0 = c_s^2 \rho_0$. With the p-representation, the pressure, p, and the velocity, $\boldsymbol{u}$, are given by

$$p = \sum_\alpha p_\alpha \tag{7}$$

$$p_0 \boldsymbol{u} = \sum_\alpha \boldsymbol{e}_\alpha p_\alpha \tag{8}$$

The incompressible LBE model proposed here consists of Eqs. (5) and (6).

Through the Chapman–Enskog procedure, the incompressible Navier–Stokes equations derived from the incompressible lattice Boltzmann model are (see Appendix for details):

$$\frac{1}{c_s^2}\frac{\partial P}{\partial t} + \nabla \cdot \boldsymbol{u} = 0 \tag{9a}$$

$$\frac{\partial \boldsymbol{u}}{\partial t} + \boldsymbol{u} \cdot \nabla \boldsymbol{u} = -\nabla P + \nu \nabla^2 \boldsymbol{u} \tag{9b}$$

where $P = p/\rho_0$, and the kinetic viscosity

$$\nu = \frac{(2\tau - 1)}{6}\frac{\delta_x^2}{\delta_t}$$

It should be noticed that Eqs. (9) are the same equations used to solve incompressible viscous Navier–Stokes equation by a finite difference method.[10]

Comments are in order at this point to justify the validity of the LBE model proposed here, which leads to Eqs. (9), to simulate incompressible Navier–Stokes equations. To do so, let us rewrite Eq. (9a) in a dimensionless form as follows:

$$\frac{1}{T}\frac{\partial P'}{\partial t'} + \frac{c_s}{L}\nabla' \cdot \boldsymbol{u}' = 0 \tag{10}$$

where $P' = P/c_s^2$, $t' = t/T$, $\nabla' = L\nabla$, $\boldsymbol{u}' = \boldsymbol{u}/c_s$, and L and T are characteristic length and time, respectively.

Clearly, in the case of steady flow, $\partial P/\partial t = 0$, thus the condition for incompressible flow, $\nabla \cdot \boldsymbol{u} = 0$, is satisfied exactly. Therefore, the only condition one must satisfy in numerical simulations of incompressible flow is

$$M \ll 1 \tag{11}$$

In practice, the condition $M < 0.15$ is usually maintained in numerical simulations by LBE method.

As to the case of unsteady flow, an additional condition must be satisfied. From Eq. (10), one can immediately see that in order for the $\partial P'/\partial t'$ term to be negligible, the following condition must be satisfied[11]:

$$T \gg L/c_s \tag{12}$$

The physical significance of the above inequality is rather clear. The time, T, during which the flow field undergoes a macroscopic change (in the range of the distance L) must be greater than the time, L/c_s, taken by a sound signal to travel the distance L, so that the propagation of interactions (by means of pressure wave or density fluctuation) in the fluid may be regarded as instantaneous (in the time scale of temporal variation of flow field).[11] Therefore, in the LBE method, the temporal variation of driving pressure should not be too fast for the above reason, and the spatial variation of pressure (or density) should not be too large for the reason of Eq. (11). Thus both conditions of Eqs. (11) and (12) must be satisfied simultaneously in simulations of unsteady incompressible flows.

III. NUMERICAL RESULTS

All the simulations described in what follows were performed on IBM RISC System/6000 590 workstations at Los Alamos National Laboratory.

A. Steady Flow: Plane Poiseuille Flow

Numerical simulations for the plane Poiseuille flow driven by either a pressure gradient or a fixed velocity profile at the entrance of channel were carried out to test the validity of the incompressible LBE model. Figure 1 shows a schematic diagram of the setup in the simulation.

At the entrance of channel (upstream), two types of boundary conditions are implemented: one is a constant pressure boundary condition, the other is a fixed velocity profile boundary condition. At the exit

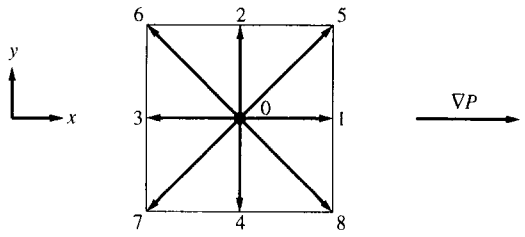

Fig. 1. All possible velocities for the 9-bit lattice BGK model on square lattice. This figure also shows the arrangement for the plane Poiseuille flow in simulations.

(downstream), a constant pressure boundary condition is applied. For the constant pressure boundary condition, the values of pressure at the entrance and the exit are set to be 1.1 and 1.0, respectively. For the fixed velocity boundary condition at the entrance, the horizontal velocity, u_x, has a parabolic profile with maximum $U_{\max} = 0.1$, whereas the vertical velocity, u_y, is zero. At the two parallel walls, a non-slip boundary condition[12] is applied. The system size is $N_x \times N_y = 17 \times 5$. Two stationary walls are located at $y = 0$ and $y = N_y - 1$, and the entrance and the exit are set at $x = 0$ and $x = N_x - 1$, respectively. The initial condition for the simulations is $\boldsymbol{u} = 0$ in the interior of the channel.

Three different values of τ, 0.75, 1.0, and 2.0, have been used in the simulations. Because the similarity of the results, only the ones with $\tau = 0.75$ are presented here. The viscosity is therefore equal to $1/12 \approx 0.0833$ with $\delta_x = \delta_t = 1$. A number of initial iterations is run to reach the steady state. The criterion of steady state is set by

$$\sum_i \frac{\|\boldsymbol{u}(\boldsymbol{x}_i, t+1) - \boldsymbol{u}(\boldsymbol{x}_i, t)\|}{\|\boldsymbol{u}(\boldsymbol{x}_i, t+1)\|} \leqslant 10^{-10}$$

where the summation is over the entire system. It usually takes a few thousand iterations to reach a steady state depending on the value of the viscosity and the boundary conditions.

Two types of measurements were taken in the simulations. One is the measurement of velocity $\boldsymbol{u}$ at several cross sections. The other is the measurement of pressure along the channel. All the measurements were taken after the steady state is attained.

Figure 2 shows the velocity profiles of u_x, with both the constant pressure and the parabolic velocity profile boundary conditions at the entrance. The velocity profiles were measured at three different cross-sections at $x = 4$, 8 and 12, respectively. The velocity profiles with the pressure gradient boundary condition (symbol ○) are normalized by the maximum velocity along the center line of the channel

$$U_{\max} = \frac{1}{8} \frac{\Delta P L_y^2}{\nu L_x} = \frac{1}{8} \frac{(P_1 - P_2) L_y^2}{\nu L_x} \tag{13}$$

where $L_y (= 4)$ and $L_x (= 16)$ are the channel width and length, $P_1 (= 1.1)$ and $P_2 (= 1.0)$ are the pressure at the entrance and the exit, respectively, and the average density $\rho_0 = 3.0$ in the simulations. As to the velocity profiles with the fixed velocity boundary condition (symbol +), they are normalized by the maximum velocity at entrance. Two types of the boundary conditions, i.e., that of a constant pressure and of a fixed parabolic

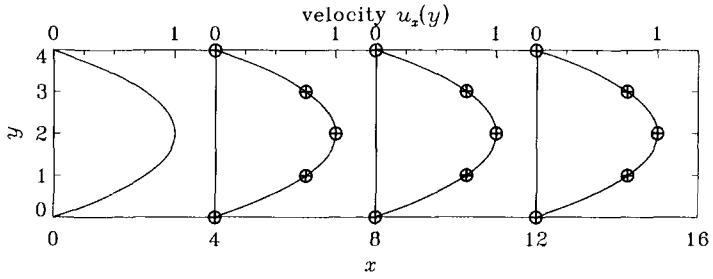

Fig. 2. The velocity profiles of $u_x(y)$ for the Poiseuille flow, with both boundary conditions of a constant pressure (○) and a fixed parabolic velocity profile of $u_x(+)$ at the entrance. The profiles of $u_x(y)$ are measured at $x = 4$, 6, and 12, respectively. All the profiles are normalized with the appropriate maximum velocity U_{max}. The solid lines in the figure are the parabolic profile of $u_x(y)$ given at the entrance and normalized by U_{max}. Note that the velocity profiles remain unchanged along the channel.

velocity profile, are equivalent in this case because of the above equation. As shown in Fig. 2, the numerical results agree with the analytical results (the solid lines) exactly.

The vertical component of the velocity, u_y, was also observed in all the simulations. The magnitude of u_y is always smaller than 10^{-10} for all cases shown here.

Figure 3 demonstrates the pressure measurements along three horizontal lines, $y = 0$, 1, and 2 (the center line of the channel). The solid line in

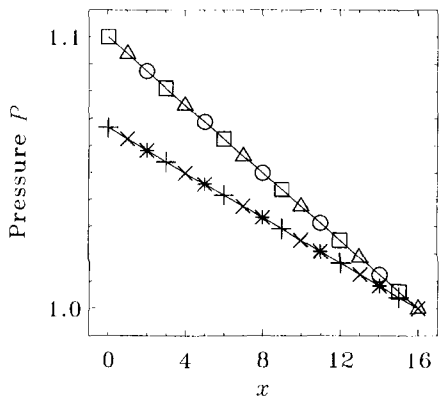

Fig. 3. Pressure distribution along the channel for the Poiseuille flow. Pressure, p, are measured at $y = 0$, 1, and 2, respectively. There are two sets of symbols to represent the results with different boundary condition at the entrance (□, △, and ○ for the constant pressure boundary condition, and +, ×, and * for the fixed velocity boundary condition). The measurements of p at $y = 1$ are taken at $x = 0$, 3,..., 12, and 15; that at $y = 1$ are taken at $x = 1$, 4,..., 13, and 16; and that at $y = 2$ are taken at $x = 2$, 5,..., 11, and 14.

the Figure is the analytic result. Clearly the numerical results agree with the analytic ones exactly for both cases with different boundary conditions. Note that the results shown in Fig. 3 are not normalized.

The combination of results shown in Figs. 2 and 3 shows that, not only the velocity profiles are correct (parabolic shape) along the channel, but also the maximum velocity of the profile is quantitatively correct. Furthermore, the pressure distribution is uniform across the channel width, and linear along the channel length. All the numerical results agree with the analytic results of the Navier–Stokes equation within the machine accuracy ($\sim 10^{-10}$). The good agreement between the numerical and analytic results is not a surprise. As shown in our analysis, the model should work well under the condition $M \ll 1$. In this particular simulation, $M_{\max} = U_{\max}/c_s = 0.15\sqrt{3} \approx 0.26 < 1.0$.

B. Unsteady Flow: 2D Womersley Flow

The two-dimensional Womersley flow (pulsatile flow in two-dimensional channel)[13, 14] is employed to validate the model for unsteady flow. The geometric configuration of the Womersley flow is identical to that of the plane Poiseuille flow, but the flow is driven by a periodic pressure gradient at the entrance of the channel.

Assuming that the flow is laminar, then the Navier–Stokes equation for the flow becomes:

$$\frac{\partial U_x}{\partial t} = -\frac{\partial P}{\partial x} + \nu \frac{\partial^2 u_x}{\partial y^2} \tag{14}$$

where the pressure gradient driving the flow is given by:

$$\frac{\partial P}{\partial x} = \mathrm{Re}[A e^{i\omega t}] \tag{15}$$

with an amplitude A and a frequency ω. The solution of the above equation is:

$$u_x(y, t) = \mathrm{Re}\left[i \frac{A}{\omega} \left(1 - \frac{\cos[\lambda(2y/L_y - 1)]}{\cos \lambda} \right) e^{i\omega t} \right] \tag{16}$$

where λ is given in terms of the Womersley number, α, as follows:

$$\lambda^2 = -i\alpha^2, \qquad \alpha^2 = \frac{L_y^2 \omega}{4\nu} \tag{17}$$

We first conducted a set of simulations of measuring velocity profiles across the channel at different times. In the simulations, the system size is $N_x \times N_y = 21 \times 21$, the period of the driving pressure is $T = 1000$ ($\omega = 2\pi/T$), and the magnitude of total pressure drop along the channel is $\Delta P = 0.001$ ($A = \Delta P/L_x$), and the pressure at the exit is set to be 1.0. The initial state of velocity field is always set to be zero everywhere in the system. The calculation of velocity field always began with $10T$ initial steps to attain convergence criterion:

$$\sum_i \frac{\|\boldsymbol{u}(\boldsymbol{x}_i, t+T) - \boldsymbol{u}(\boldsymbol{x}_i, t)\|}{\|\boldsymbol{u}(\boldsymbol{x}_i, t+T)\|} \leqslant 10^{-7}$$

where the summation is over the entire system.

Figure 4 shows the velocity profiles across a section of the channel at $x = 10$ at four different times after the initial run: $t = T/8$, $T/4$, $3T/8$, and $T/2$. The relaxation time τ is chosen to be 0.6178. With the above parameters, the Womersley number $\alpha \approx 4.0$. The agreement between the numerical and analytical results given by Eq. (16) is excellent.

Figure 5 shows the normalized maximum velocity along the center of the channel, $U_c/U_{\max}$, where $U_{\max}$ is given by Eq. (13), and the phase lag of the velocity field, θ (normalized by π), as functions of the Womersley number, α. The Womersley number, α, is varied via adjusting τ. The analytic results represented by the solid (θ/π) and the dashed ($U_c/U_{\max}$) line in the figure are derived from Eq. (16). The numerical results are in excellent agreement with the analytic ones.

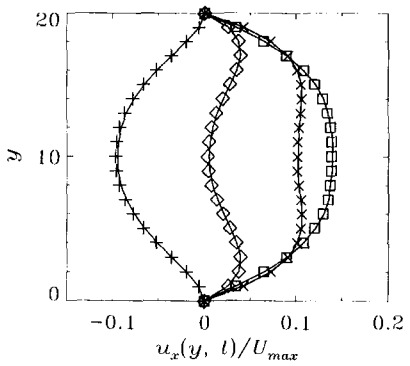

Fig. 4. Normalized velocity profiles, $u_x(y, t)/U_{\max}$, of Womersley flow with $\alpha \approx 4.0$. The measurements were taken at the middle of the channel, $x = 10$, at fours different times after initial run at: $t = T/8$ (+), $T/4$ ($\diamond$), $3T/8$ ($\times$), and $T/2$ ($\square$). The solid lines are analytic result given by Eq. (16).

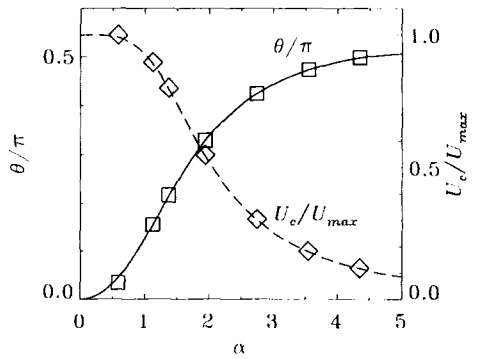

Fig. 5. Normalized Maximum velocity at the center of the channel, $U_c/U_{\max}$, ($\diamond$), and the phase lag of the velocity ($\square$) normalized by π, θ/π, vs. the Womersley number α. The solid line (θ/π) and dashed line ($U_c/U_{\max}$) are analytic result obtained from Eq. (16).

To compare the incompressible LBE model with previous models, we compute the relative global error in velocity field of simulations against analytical results as a function of the pressure drop, ΔP (or the maximum Mach number $M_{\max}$). The parameters in this particular simulation are: $T=2000$, $\tau=0.75$, and $N_x \times N_y = 21 \times 21$. Table I shows the error measured with L^2 norm:

$$\|\delta \boldsymbol{u}\|^q = \frac{\sum_i \|\boldsymbol{u}(\boldsymbol{x}_i, t) - \boldsymbol{u}_0(\boldsymbol{x}_i, t)\|^q}{\sum_i \|\boldsymbol{u}_0(\boldsymbol{x}_i, t)\|^q} \tag{18}$$

where the summation is over the entire system, $\boldsymbol{u}_0$ is the analytic solution given by Eq. (16), and $q=2$. In Table I, L_I^2 is the relative global error of

Table I. The Relative Global Error of Velocity Field in 2-D Womersley Flow[a]

ΔP	$M_{\max}$	L_I^2	L_C^2
0.001	0.0094	0.29%	0.29%
0.005	0.047	0.63%	0.72%
0.01	0.094	1.20%	1.54%
0.02	0.188	2.34%	3.63%
0.05	0.471	5.73%	12.50%

[a] The system size $N_x \times N_y = 21 \times 21$. The relaxation time $\tau = 0.6178$. ΔP, $M_{\max}$ are the magnitude of total pressure gradient and maximum Mach number, respectively. L_I^2 and L_C^2 are the relative global error, measured with L^2 norm, by using incompressible and compressible LBE model, respectively.

the simulation by using the incompressible LBE model proposed in this paper, whereas L_C^2 is the error by using the existing LBE model. The measurements of the error were conducted similarly to the preceding simulations. All simulations for the measurement began with an initial condition of zero velocity every where, and an initial run of $10T$ steps, with a given value of ΔP, to obtain $\boldsymbol{u}$. Then the analytic solution, $\boldsymbol{u}_0$, at the corresponding time can be constructed according to Eq. (16). The error was then computed according to Eq. (18). The measurement was repeated by varying the value of ΔP. We also changed the number of steps in the initial run to detect time-dependence of the error. Our observation shows that the error is time-independent, although it fluctuates slightly.

It is known that to maintain the incompressible limit, the density fluctuation $\delta\rho$ must be of the order $O(M^2)$.[9] Therefore, with small pressure drop ΔP, the errors of the two models are comparable, because density variation $\delta\rho$ is very small such that the error due to compressible effect is negligible compared to error due to other effects (e.g., discretization) under the circumstance. However, the error in previous LBE model (L_C^2) grows faster as ΔP increases. (Assuming $\|\delta\boldsymbol{u}\| \sim aM_{\max}^{\gamma}$, then the values of γ for L_I^2 and L_C^2 are 0.9591 ± 0.0074, and 1.242 ± 0.041 in the range $0.047 \leqslant M_{\max} \leqslant 0.471$, respectively.) In the simulation, because $T = 2000 \gg L_x/c_s = 20\sqrt{3} \approx 35$, therefore the compressible effect due to the time variation of pressure field, which is proportional to $L_x/c_s T \approx 10^{-2}$, is in fact negligible.

We have also observed that as T decreases, the error increases. Figure 6 shows the dependence of the relative global error in L^2 norm on T. In

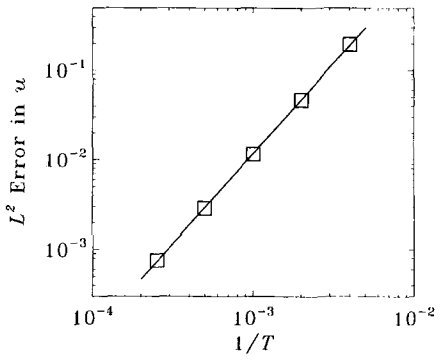

Fig. 6. L^2-normed relative global error of $\boldsymbol{u}$ vs. $1/T$ for the Womersley flow. Symbol □ presents the numerical results, and solid line presents the least-squared fitting of the data. The parameters in the simulations are: $\alpha = 1.94$ and $M_{\max} = 0.0094$. With these given values of α and $M_{\max}$, $\tau = (T + 1000)/2T$, and $\Delta P = 2/T$. The values of T used in the simulation are 250, 500, 1000, 2000, and 4000.

this set of simulations, $\alpha = 1.94$ and $M_{\max} = 0.0094$. With above given values of α and $M_{\max}$,

$$\tau = \frac{T + 1000}{2T}, \qquad \Delta P = \frac{2}{T} \tag{19}$$

The values of T used in the simulation are 250, 500, 1000, 2000, and 4000. Our analysis shows that the error grows as T^{-2}. The numerical result in Fig. 6 gives the value of the exponent 2.008 ± 0.012. We also measured the L^1-normed error. The value of the exponent measured from the L^1-normed error ($q = 1$ in Eq. (18)) is 1.993 ± 0.017.

IV. DISCUSSION AND CONCLUSION

We have proposed a lattice Boltzmann model for the incompressible hydrodynamics and derived the incompressible Navier–Stokes equations through the Chapman–Enskog procedure with rigor. The compressible effect has been reduced in the incompressible lattice Boltzmann model. This is accomplished by eliminating the terms of the order $o(M^2)$, where M is the Mach number. The approximation made is entirely consistent with the second order low Mach number expansion in the Chapman–Enskog analysis of LBE models.

We have also performed numerical simulations for the plane Poiseuille flow (steady flow) with different boundary conditions at the entrance, and the 2-D Womersley flow (unsteady flow) using the incompressible Boltzmann model. For the Poiseuille flow, we have computed the velocity profile in several cross-sections of channel, and measured the pressure distribution along and across the channel. Our simulations have shown that the velocity profile is remained unchanged (as a parabolic profile) along the channel, and that the pressure distribution is linear along the channel and uniform across the channel. All these results are simultaneously in excellent agreement with the analytical solutions of the Navier–Stokes equation. Our numerical results are accurate within the machine precision.

As to the Womersley flow, the velocity profile as a function of time and space was computed. The phase lag of the velocity field and the amplitude of the velocity profile as functions of the Womersley number, α, were also measured. All these numerical results accurately agreed with analytic results obtained in Eq. (16).

The model proposed here is mathematically equivalent to the model in ref. 8 provided that $\rho_0 = 1$. However, it is important to point out the distinction between the incompressible LBE model proposed here and the previous ones based upon the j-representation ($\boldsymbol{j} \equiv \rho \boldsymbol{u}$).[6,8] First of all, the previous

models based upon the j-representation[6-8] can not lead to the genuine incompressible Navier–Stokes equations in general. Second, the argument of the j-representation is only valid for steady flows. In our model, the compressible effect of the order $o(M^2)$ is explicitly eliminated. The model proposed here is valid for steady as well as unsteady flows.

In conclusion, we have developed an incompressible LBE model to recover the incompressible Navier–Stokes equations. The compressible effect in the previous LBE models has been reduced effectively. Furthermore, our incompressible LBE model is valid in general for both steady and unsteady flows. We hope this work would encourage wider applications of the LBE method in hydrodynamic simulations in the CFD community.

APPENDIX: CHAPMAN–ENSKOG DERIVATION OF THE NAVIER–STOKES EQUATION

By introducing the following expansions[9]:

$$f_\alpha(\boldsymbol{x}+\boldsymbol{e}_\alpha\delta_t, t+\delta_t)=\sum_{n=0}^{\infty}\frac{\varepsilon^n}{n!}D_t^n f_\alpha(\boldsymbol{x}, t) \tag{A1a}$$

$$f_\alpha=\sum_{n=0}^{\infty}\varepsilon^n f_\alpha^{(n)} \tag{A1b}$$

$$\partial_t=\sum_{n=0}^{\infty}\varepsilon^n\partial_{t_n} \tag{A1c}$$

where $\varepsilon=\delta_t$ and $D_t\equiv(\partial_t+\boldsymbol{e}_\alpha\cdot\nabla)$, we can rewrite the lattice Boltzmann equation

$$f_\alpha(\boldsymbol{x}+\boldsymbol{e}_\alpha\delta_t, t+\delta_t)-f_\alpha(\boldsymbol{x}, t)=-\frac{1}{\tau}[f_\alpha(\boldsymbol{x}, t)-f_\alpha^{(\mathrm{eq})}(\boldsymbol{x}, t)] \tag{A2}$$

in the consecutive order of the parameter ε as follows:

$$O(\varepsilon^0):\quad f_\alpha^{(0)}=f_\alpha^{(\mathrm{eq})} \tag{A3a}$$

$$O(\varepsilon^1):\quad D_{t_0}f_\alpha^{(0)}=-\frac{1}{\tau}f_\alpha^{(1)} \tag{A3b}$$

$$O(\varepsilon^2):\quad \partial_{t_1}f_\alpha^{(0)}+\left(\frac{2\tau-1}{2\tau}\right)D_{t_0}f_\alpha^{(1)}=-\frac{1}{\tau}f_\alpha^{(2)} \tag{A3c}$$

where $D_{t_n} \equiv (\partial_{t_n} + \boldsymbol{e}_\alpha \cdot \nabla)$, and note that Eq. (A3b) has been substituted into Eq. (A3c). The distribution function f_α is the normal solution which is constrained by:

$$\sum_\alpha f_\alpha^{(0)} \begin{bmatrix} 1 \\ \boldsymbol{e}_\alpha \end{bmatrix} = \begin{bmatrix} \rho \\ \rho_0 \boldsymbol{u} \end{bmatrix} \tag{A4a}$$

$$\sum_\alpha f_\alpha^{(n)} \begin{bmatrix} 1 \\ \boldsymbol{e}_\alpha \end{bmatrix} = 0, \qquad n > 0 \tag{A4b}$$

where the equilibrium $f_\alpha^{(0)}$ is defined by Eq. (4) (for the 9-bit model):

$$f_\alpha^{(\mathrm{eq})}(\boldsymbol{x}, t) = \omega_\alpha \left\{ \rho + \rho_0 \left[3 \frac{(\boldsymbol{e}_\alpha \cdot \boldsymbol{u})}{c^2} + \frac{9}{2} \frac{(\boldsymbol{e}_\alpha \cdot \boldsymbol{u})^2}{c^4} - \frac{3}{2} \frac{\boldsymbol{u}^2}{c^2} \right] \right\} \tag{A5}$$

Also, f_α is a Chapman–Enskog *ansatz*, i.e., the time dependent of f_α is through the hydrodynamic variables ρ and $\boldsymbol{u}$ (and temperature T if applied). Therefore,

$$\partial_t f_\alpha = \frac{\partial f_\alpha}{\partial \rho} \partial_t \rho + \frac{\partial f_\alpha}{\partial \boldsymbol{u}} \partial_t \boldsymbol{u} \tag{A6}$$

For the 9-bit model, the tensor

$$E^{(n)} = \sum_{\alpha \neq 0} \omega_\alpha \boldsymbol{e}_{\alpha,1} \boldsymbol{e}_{\alpha,2} \cdots \boldsymbol{e}_{\alpha,n} \tag{A7}$$

where $\boldsymbol{e}_{\alpha,i}$ is the projection of $\boldsymbol{e}_\alpha$ on i-axis ($i = x$, or y), has the following properties:

$$E^{(2)} = \sum_{\alpha \neq 0} \omega_\alpha \boldsymbol{e}_{\alpha,i} \boldsymbol{e}_{\alpha,j} = \tfrac{1}{3} c^2 \delta_{ij} \tag{A8a}$$

$$E^{(4)} = \sum_{\alpha \neq 0} \omega_\alpha \boldsymbol{e}_{\alpha,i} \boldsymbol{e}_{\alpha,j} \boldsymbol{e}_{\alpha,k} \boldsymbol{e}_{\alpha,l} = \tfrac{1}{9} c^4 \Delta_{ijkl} \tag{A8b}$$

because

$$\sum_{\alpha=1}^{4} \boldsymbol{e}_{\alpha,i} \boldsymbol{e}_{\alpha,j} = 2c^2 \delta_{ij} \tag{A9a}$$

$$\sum_{\alpha=5}^{8} \boldsymbol{e}_{\alpha,i} \boldsymbol{e}_{\alpha,j} = 4c^2 \delta_{ij} \tag{A9b}$$

$$\sum_{\alpha=1}^{4} e_{\alpha,i} e_{\alpha,j} e_{\alpha,k} e_{\alpha,l} = 2c^4 \delta_{ijkl} \tag{A9c}$$

$$\sum_{\alpha=5}^{8} e_{\alpha,i} e_{\alpha,j} e_{\alpha,k} e_{\alpha,l} = 4c^4 \Delta_{ijkl} - 8c^2 \delta_{ijkl} \tag{A9d}$$

where δ_{ij} and δ_{ijkl} are the Kronecker delta with two and four indices, respectively, and

$$\Delta_{ijkl} = \delta_{ij}\delta_{kl} + \delta_{ik}\delta_{jl} + \delta_{il}\delta_{jk} \tag{A10}$$

Also, $E^{(2n+1)} = 0$ for $n = 0, 1, \ldots$.

With the above properties of the tensor $E^{(n)}$, we have:

$$\sum_{\alpha} f_{\alpha}^{(0)} = \rho \tag{A11a}$$

$$\sum_{\alpha} e_{\alpha} f_{\alpha}^{(0)} = \rho_0 \boldsymbol{u} \tag{A11b}$$

$$\sum_{\alpha} e_{\alpha,i} e_{\alpha,j} f_{\alpha}^{(0)} = \tfrac{1}{3} c^2 \rho \delta_{ij} + \rho_0 u_i u_j \tag{A11c}$$

$$\sum_{\alpha} e_{\alpha,i} e_{\alpha,j} e_{\alpha,k} f_{\alpha}^{(0)} = \tfrac{1}{3} c^2 \rho_0 (\delta_{ij} u_k + \delta_{ki} u_j + \delta_{jk} u_i) \tag{A11d}$$

The moments of Eq. (A3b) lead to the Euler equations

$$\partial_{t_0} \rho + \nabla \cdot (\rho_0 \boldsymbol{u}) = 0 \tag{A12a}$$

$$\partial_{t_0} (\rho_0 \boldsymbol{u}) + \nabla \cdot \Pi^{(0)} = 0 \tag{A12b}$$

where $\Pi^{(0)} = \sum_{\alpha} e_{\alpha} e_{\alpha} f_{\alpha}^{(0)}$ is the zeroth-order momentum flux tensor. With $\Pi_{ij}^{(0)}$ given by Eq. (A11c), the above equations can be rewritten as:

$$\frac{1}{c_s^2} \partial_{t_0} P + \nabla \cdot \boldsymbol{u} = 0 \tag{A13a}$$

$$\partial_{t_0} \boldsymbol{u} + \boldsymbol{u} \cdot \nabla \boldsymbol{u} = -\nabla P - \boldsymbol{u} \nabla \cdot \boldsymbol{u} \tag{A13b}$$

where $P = c_s^2 \rho / \rho_0$ is the normalized pressure, and $c_s = c/\sqrt{3}$. It should be pointed out that the divergent term is canceled out *exactly* in other standard LBE models, whereas in the model here, the divergent term, $\boldsymbol{u} \nabla \cdot \boldsymbol{u}$, remains in the momentum equation. Nevertheless, with Eq. (A13a), the divergent term in Eq. (A13b) is indeed of order $O(M^3)$, which is a higher order term in contrast with other terms in Eq. (A13b).

The moments of Eq. (A3c) lead to the following equations:

$$\partial_{t_1}\rho = 0 \tag{A14a}$$

$$\partial_{t_1}(\rho_0 \boldsymbol{u}) + \frac{(2\tau - 1)}{2\tau}\nabla \cdot \Pi^{(1)} = 0 \tag{A14b}$$

where $\Pi^{(1)} = \sum_\alpha \boldsymbol{e}_\alpha \boldsymbol{e}_\alpha f_\alpha^{(1)}$ is the first-order momentum flux tensor. With the aid of Eqs. (A11) and (A13), we have:

$$\begin{aligned}
\Pi_{ij}^{(1)} &= \sum_\alpha \boldsymbol{e}_{\alpha,i}\boldsymbol{e}_{\alpha,j} f_\alpha^{(1)} = -\tau \sum_\alpha \boldsymbol{e}_{\alpha,i}\boldsymbol{e}_{\alpha,j} D_{t_0} f_\alpha^{(0)} \\
&= -\tau[\partial_{t_0}\Pi_{ij}^{(0)} + \tfrac{1}{3}c^2\rho_0(\nabla\cdot\boldsymbol{u}\,\delta_{ij} + \nabla_i u_j + \nabla_j u_i)] \\
&= -\tau[\rho_0\partial_{t_0}(u_i u_j) + c_s^2\rho_0(\nabla_i u_j + \nabla_j u_i)] \\
&= \tau[c_s^2(u_i\rho + u_j\nabla_i\rho) + \rho_0(u_i(\boldsymbol{u}\cdot\nabla)\,u_j + u_j(\boldsymbol{u}\cdot\nabla)\,u_i) - c_s^2\rho_0(\nabla_i u_j + \nabla_j u_i)]
\end{aligned} \tag{A15}$$

where $\nabla_i = \partial/\partial x_i$. In the above result, the terms of $O(\boldsymbol{u}^3)$ should be neglected, in order to be consistent with the small velocity expansion of $f_\alpha^{(\mathrm{eq})}$ up to the order of $O(\boldsymbol{u}^2)$ (Note that $O(\boldsymbol{u}) = O(M)$, therefore we take the liberty to interchange these notations.) Also, the terms of $u_i\nabla_j\rho$ should be neglected because they are of the order $O(M^3)$. Therefore,

$$\begin{aligned}
\frac{(2\tau-1)}{2\tau}\nabla_j\Pi_{ij} &= -\frac{\nu}{\delta_t}\rho_0\nabla_j(\nabla_i u_j + \nabla_j u_i) + O(M^3) \\
&= -\frac{\nu}{\delta_t}\rho_0(\nabla_i\nabla\cdot\boldsymbol{u} + \nabla^2 u_i) + O(M^3) \\
&= -\frac{\nu}{\delta_t}\rho_0\nabla^2 u_i + O(M^3)
\end{aligned} \tag{A16}$$

where the term $\nabla\cdot\boldsymbol{u}$ has been neglected because it is of $O(M^2)$ due to Eq. (A13a), and the viscosity

$$\nu = \frac{(2\tau-1)}{6}\frac{\delta_x^2}{\delta_t}$$

Combining the zeroth and first order results together with $\partial_t = \partial_{t_0} + \varepsilon\,\partial_{t_1}$, and setting the expansion parameter $\varepsilon = 1$ eventually, we have

the incompressible Navier–Stokes equations accurate to the order of $O(M^2)$ in continuity equation and $O(M^3)$ in momentum equation:

$$\nabla \cdot \mathbf{u} = 0 + O(M^2) \tag{A17a}$$

$$\frac{\partial \mathbf{u}}{\partial t} + \mathbf{u} \cdot \nabla \mathbf{u} = -\nabla P + \nu \nabla^2 \mathbf{u} + O(M^3) \tag{A17b}$$

It should be stressed that in deriving Eq. (A17b), an approximation is made to neglect the terms of higher order than the convection term of order $O(M^2)$, in particular, the divergent term (compressibility).

ACKNOWLEDGMENTS

The authors would like to thank Dr. Gary D. Doolen and Dr. Micah Dembo of LANL for their support and encouragement during this work. The authors would also like to express their gratitude to Prof. D. d'Humières for his diligence in reviewing this paper and his constructive and insightful suggestions and comments. XYH would like to thank Prof. Q. Zou, and LSL to Prof. C. D. Levermore, for helpful discussions.

REFERENCES

1. G. McNamara and G. Zanetti, *Phys. Rev. Lett.* **61**:2332 (1988).
2. H. Chen, S. Chen, and W. H. Matthaeus, *Phys. Rev. A* **45**:R5339 (1991).
3. Y. H. Qian, D. d'Humières, and P. Lallemand, *Europhys. Lett.* **17**:479 (1992).
4. Gary D. Doolen, ed., *Lattice Gas Methods for Partial Differential Equations* (Addison–Wesley, Redwood City, California, 1990).
5. R. Benzi, S. Succi, and M. Vergassola, *Phys. Rep.* **222**:145 (1992).
6. U. Frisch, D. d'Humières, B. Hasslacher, P. Lallemand, Y. Pomeau, and J.-P. Rivet, *Complex Systems* **1**:649 (1987).
7. F. J. Alexander, H. Chen, S. Chen, and G. D. Doolen, *Phys. Rev. A* **46**:1967 (1992).
8. Q. Zou, S. Hou, S. Chen, and G. D. Doolen, *J. Stat. Phys.* **81**:35 (1995).
9. L.-S. Luo, Ph.D. thesis, Georgia Institute of Technology (1993).
10. A. J. Chorin, *J. Comp. Phys.* **2**:12 (1967).
11. L. D. Landau and E. M. Lifshitz, *Fluid Mechanics*, 2nd Edition, (Pergamon, Elmsford, New York, 1987).
12. X. He, Q. Zou, L.-S. Luo, and M. Dembo, *J. Stat. Phys.* **87**:115 (1997).
13. J. R. Womersley, *J. Physiol.* **127**:553 (1955).
14. I. G. Currie, *Fundamental Mechanics of Fluids*, (McGraw-Hill, New York, 1974).